Molecular Simulations of the Interlamellar Phase in Polymers: Effect of Chain Tilt

S. Gautam, S. Balijepalli,† and G. C. Rutledge*

Department of Chemical Engineering and Center for Materials Science and Engineering, Massachusetts Institute of Technology, Cambridge, Massachusetts 02139

Received July 18, 2000; Revised Manuscript Received September 19, 2000

ABSTRACT: Semicrystalline polymers exhibit metastable interphases, which must simultaneously accommodate molecular connectivity and disorder across the interlamellar phase. Off-lattice molecular simulations, previously used to study the {001} interphase in freely rotating chains, are used here to study the interlamellar phases between the {101}, {201}, and {502} crystal facets (polymer chains tilted to the lamellar normal by 19°, 34.4°, and 41°, respectively). The order-to-disorder transition from the crystal to the amorphous region occurs with an interface approximately 10−12 Å thick, for all cases studied. The interfacial potential energies for the {101}, {201}, and {502} facets are computed to be 100, 70, and 90 mJ/m^2, respectively, compared to 140 mJ/m^2 for the {001} facet. The topology in the interlamellar phase shifts away from tight folding as the tilt angle of the chains exiting the crystal increases. Whereas [110] loops dominate the {001} interface, loop reentry along [200] and [310] directions is more common in the interfaces with tilted chains. The chain length distributions associated with tilted chains more closely approximate the ideal distribution suggested by a model of Gaussian chains, which indicates that entropy favors tilting of polymer chains away from the lamellar normal. These results are consistent with the frequent observation of {201} oriented interfaces in polyethylene and offer a thermodynamic explanation for the selection of interface orientation in semicrystalline polyethylene.

1. Introduction

On a molecular scale, semicrystalline polymers consist of crystalline and amorphous regions that are interconnected by molecular chains that participate in both regions.[1] A popular model for such materials consists of chains threading through stacks of alternating crystalline and amorphous phases, separated by an interface. The "interface" is the partially ordered transition zone close to the lamellar surfaces, while the entire region of noncrystalline material between lamella (including the amorphous region and the interfaces) is referred to as the interlamellar phase, or "interphase".[2,3] The morphology of semicrystalline polymer interphases has been the subject of intensive study over the years. The detailed structure and thermodynamics of the crystal−amorphous interphase contribute to various mechanical and thermal properties and play an important role in determining the ultimate behavior of the polymer.

Several studies have been performed in an attempt to understand the interphase structure. It is well-established now that polyethylene shows a crystal lamellar structure and that there is chain folding in the interphase region.[4] One of the important observed features, which is also the focus of the present study, is that the polymer chain stems are not generally orthogonal to the basal plane of the lamellae. In this article, such basal planes are identified by chain tilt angle, defined as the angle between the lamellar normal and the direction of polymer chain stems, as has been done by various authors in the past.[5−8] Detailed investigations by Frank and Bolz[9] showed that the molecular chains are inclined up to 30° from the lamellar normal in some cases. Basset and Hodge[10−13] studied polyethylene spherulites using electron microscopy and found a regular texture showing well-defined lamellae having crystal stems inclined at an angle ranging from 19° to 41° to the lamellar normal, with 34° (corresponding to the {201} facet) being the most common. Voigt-Martin[14] also concluded from electron microscopy data that most of the polyethylene lamellae exhibit basal planes of the type {*h*0*l*}. Khoury[5] observed the presence of a predominant chain tilt angle of ∼34° in polyethylene spherulites grown from the melt at high undercoolings, through dark-field scanning transmission electron microscopy. Although chain tilt angles higher than 45° have also been reported,[15,16] these studies involved special conditions of sample preparation. Keith and Padden[6,17,18] discussed growth habits in melt-crystallized polyethylene and attributed slower crystallization kinetics to a tilted-chain growth front. They also argued that the nonorthogonality of lateral growth faces and fold surfaces leads to the development of different degrees of disorder at the opposite fold surfaces, which in turn give rise to the observed phenomenon of lamellar twisting. Lovinger and Keith[19] showed through the example of α-phase poly(vinylidene fluoride) that chain tilt is virtually assured in lamellar crystals having triclinic or monoclinic symmetry.

These experimental studies, however, do not resolve the detailed structure or explain the origin of properties in the interfacial region. Molecular simulation offers a promising avenue for predicting structural, conformational, and thermodynamic properties in this regard. Various theoretical models like random walk models[20,21] and lattice models based on mean field theory[22−24] as

† Current address: Dow Chemical Company, Midland, MI 48642.

* Corresponding author: e-mail rutledge@mit.edu.

10.1021/ma0012503 CCC: $19.00
Published on Web 11/05/2000

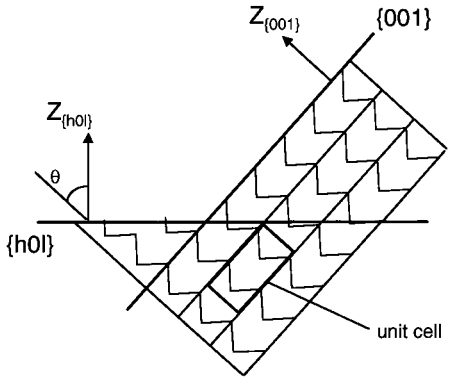

Figure 1. Illustration of chain tilt angle (θ) and basal plane orientation for $\{h0l\}$ interphases. $z_{\{001\}}$ lies parallel to the crystallographic *c*-axis and normal to the {001} plane. $z_{\{h0l\}}$ is tilted at an angle θ with respect to $z_{\{001\}}$ in the $x-z$ plane and defines the normal to the $\{h0l\}$ plane. Zigzag polyethylene conformations are indicated schematically.

well as Monte Carlo techniques[25,26] have been employed in the past. However, these models do not capture the realistic effect of chain architecture and geometry. We have recently reported[2,3] the results of an off-lattice Monte Carlo simulation to study the structure and thermodynamics of the interphase region, using realistic potentials of interaction. This model accounted for the dissipation of order and density across the interface. In these initial simulations, however, the chain stems exiting from the crystal were taken to be orthogonal to the interface, a simplifying assumption in accord with prevailing crystallization theories, but at odds with the aforementioned experimental studies.

Tilting of chain stems has long been known to exert a strong influence on the structure and properties of the interface. Frank[27] suggested long ago that mutual exclusion imposes steric constraints on the structure of the interface between crystalline and amorphous regions that is only relieved by the presence of chain ends, backfolding, and chain tilt. Yoon and Flory[7] and Kumar and Yoon[23] also considered the reduction of flux of chains to the amorphous region due to chain tilt and its effect on chain folding. Mandelkern[8] suggested further that the chain tilt angle is an important factor in any detailed description of crystallization mechanism and that it also influences the interfacial free energy associated with the basal plane. Basset et al.[11] and Keith and Padden[6] discussed the role of tilted growth of polymer crystals in allowing better packing and enhanced space for accommodation of disordered conformations and relatively bulky loops within interfacial layers.

In this work we report the study of tilted-chain interphases using off-lattice Monte Carlo simulation. In experimental studies, the most commonly observed interfaces (and the corresponding tilt angles) are {101} interface (19°), {201} interface (34.4°), and {502} interface (41°). The correspondence between chain tilt and Miller indices for the interface is demonstrated through Figure 1. We performed our simulations on {101}, {201}, and {502} interfaces and compared with the {001} interface to understand the underlying causes for chain tilt and to quantify the impact of chain tilt on structure and properties. The organization of the article is as follows. The methodology is discussed in the next section, where we have explained the molecular model, the generation of initial structure, and the simulation details. Section 3 discusses the characterization of the structure and properties of the system. Section 4 discusses the results, and the conclusion is presented in section 5.

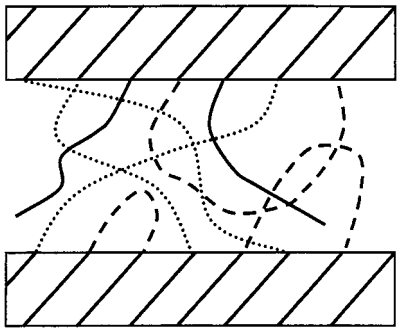

Figure 2. Schematic diagram of the interphase, showing the examples of loops (dashed), bridges (dotted), and tails (solid).

2. Simulation Methodology

Figure 2 illustrates the interphase with chain populations of three types: "bridges" that join two crystal lamellae, "loops" that have their entry and exit points on the same crystal lamella, and "tails" that terminate in the amorphous phase. The polymer is modeled as chains of united atoms with fixed bond lengths (1.53 Å) and fixed bond angles (112°). In accord with our previous reports,[2,3] no explicit torsion potential is used, thereby resulting in a freely rotating chain model. The nonbonded interaction between united atoms was calculated using a truncated Lennard-Jones shifted force potential with $\sigma = 3.94$ Å and $\epsilon/k_b = 49.3$ K,[28] typical of CH_2 groups. Nonbonded interactions along the same chains were calculated between atoms separated by more than three bonds. The cutoff radius for interactions was defined as $L_{min}/2$ where L_{min} is the length of the smallest side of the simulation box. The temperature of the simulation was maintained at 450 K, which is a little higher than the melting point of polyethylene.

The simulation box size is three unit cells in the *x*- and *y*-directions, and as large a dimension as necessary along *z* to ensure an amorphous centerline in the simulation. The unit cell is orthorhombic with $a = 7.40$ Å, $b = 4.93$ Å, and $c = 2.54$ Å, typical of polyethylene. The corresponding box sizes were $23.5 \times 14.7 \times 46.2$ Å for the {101} interface, $26.9 \times 14.7 \times 46.6$ Å for the {201} interface, and $29.4 \times 14.7 \times 46.9$ Å for the {502} interface. The top and bottom faces of the simulation box in the *z*-direction correspond to the crystal lamellae. Polymer chains emanate from both the top and bottom surface along the direction of chain tilt and contribute to the interphase. The three beads in each chain closest to the crystal surface are fixed in crystallographic registry and represent explicitly the first three crystallographic layers. Periodic boundary conditions were imposed in the *x*- and *y*-directions, and long-range corrections in the *z*-direction were computed using the Steele potential, as described elsewhere.[29] The Monte Carlo simulation was performed in the (N, n, V, T, μ_i*) ensemble, in which the total number of chains (N), total number of atoms (n), volume (V), and temperature (T) of the simulation were fixed. For chain segments of different lengths, the chemical potential per bead was also assumed to be constant (i.e., reduced chemical potential $\mu_i^* = 0$), as suggested by Kumar et al.[30]

Four Monte Carlo moves were utilized to sample the configuration space, by changing both the local confor-

mations of the chains and the topology of the interphase. End-rotation, reptation, and intrachain concerted rotation moves sample changes in conformation and packing, while the end-bridging move samples both conformational and topological changes and serves to equilibrate the conformational characteristics of chains at larger length scales, for example, at the level of end-to-end distance. The end-rotation move performs a simple rotation of one to three atoms at the end of a tail. In the reptation move, an end segment of a tail is removed and appended to another tail with a randomly selected torsion angle. The intrachain concerted rotation algorithm was initially developed by Dodd et al.[28] and is adopted here to effect significant local rearrangements to the interior of chains. The move consists of excising a randomly selected group of four skeletal atoms internal to the polymer chain and then reconstructing the group of atoms such that the translational and rotational constraints required to reconnect the two parts of the chain are satisfied. The end-bridging move[31] utilizes the concerted rotation algorithm as well. The end-bridging move takes a pair of a bridge and a tail, or a loop and a tail, and changes both the topology and conformation of those pairs. For example, a bridge and a tail can be transformed to a different bridge and a tail or to a loop and a tail. This connectivity-altering move greatly enhances the efficiency with which widely different molecular configurations are sampled, thus providing a powerful tool to equilibrate structure. In addition, this move is essential to introduce changes in topology of the interphase. For the present simulations, the moves were attempted in the ratio of 1:1:5:20 of rotation, reptation, intrachain concerted rotation, and end-bridging.

The initial structure is generated in the all-trans orthorhombic crystalline structure of polyethylene. We applied Euler angle rotations to this structure, to obtain tilted chains with a specific monoclinic angle. A number of atoms are removed to establish the density of the simulation box intermediate to the crystal density of 1 g/cm^3 and amorphous density of 0.84 g/cm^3. The removal of atoms also results in the introduction of tails and loops in the system. To obtain the corresponding number density, atoms were removed by cutting chains using an interchain variant of the concerted rotation algorithm that permits topological transformations on bridge−bridge, loop−loop, or bridge−loop pairs.[29] Removal of atoms is an important step to generate a metastable configuration, which is subsequently unable to relax toward either a completely amorphous or a completely crystalline phase. The boundaries are constrained to be crystalline, but the density constraint ensures that the center of the cell is amorphous. Hence, a frustrated system results, which samples the metastable equilibrium state through Monte Carlo moves.

The simulation length was chosen to ensure acquisition of a statistical sample of uncorrelated configurations. Autocorrelation functions for the end-to-end vector of a chain segment were used to quantify the sampling of configuration space. The first and second moments are given by

$$m_1(\tau) = \langle \mathbf{u}_i(t)\cdot\mathbf{u}_i(t+\tau)\rangle$$

$$m_2(\tau) = (3\langle(\mathbf{u}_i(t)\cdot\mathbf{u}_i(t+\tau))^2\rangle - 1)/2 \qquad (1)$$

A double averaging is performed over all the chains in the system (subscripts i) and all configurations (brackets). Here, $\mathbf{u}_i$ is the end-to-end unit vector for the ith chain, and $(t, t+\tau)$ refer to configurations separated by τ Monte Carlo steps. These moments are a measure of how fast the memory of a previous local configuration is lost. The moments are equal to 1 when $\tau = 0$ and decay to zero as τ goes to ∞. An exponential fit to the autocorrelation function $m_1(\tau)$ for the {201} interphase is shown in Figure 3. Its long-time behavior decays with a half-life of about 0.7 million moves. Approximately 5 million Monte Carlo moves were used to equilibrate the initial structure, followed by 15 million moves of actual simulation. Configurations were saved after every 2000 moves, to calculate the averages for quantitative properties.

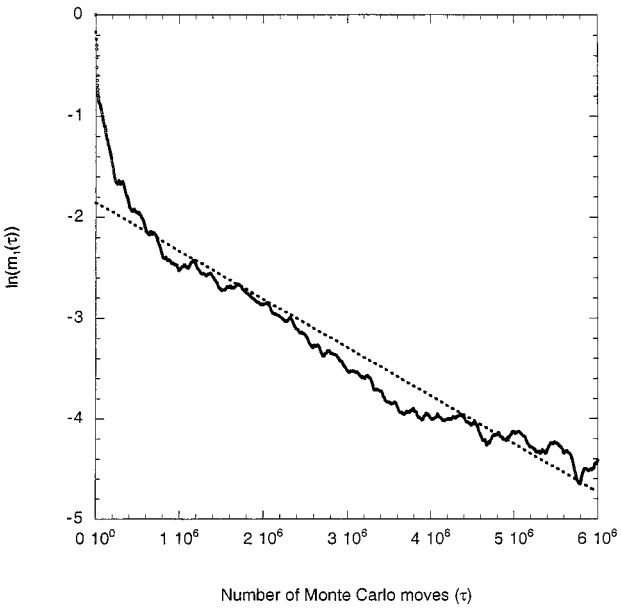

Figure 3. Autocorrelation function for first moment of the end-to-end vector of chains segments is shown for {201} interphase. The dotted line is the linear curve fit to the long "time" behavior.

3. Characterization of Structure and Properties

To characterize the interphase structure, the simulation box was divided into slices normal to the z-axis (referred to as "bins"). The width of each bin was taken to be about 1/10 of the crystal C−C bond length, projected onto the z-axis. We calculated the structural properties for each bin as described below. These properties were then averaged over all the configurations to get the ensemble averages.

The density of each bin was computed by adding the volume contributions from each atom and normalizing by the occupied atomic volume of an equivalent bin in the crystal. The volume contribution of a single atom of diameter σ, which is intersected by a bin having its boundaries at distances z_1 and z_2 from the center of the atom, is given by the following equation:

$$v = \frac{\pi}{3}(z_2 - z_1)\left(\frac{3\sigma^2}{4} - [z_1^2 + z_2^2 + z_1 z_2]\right) \qquad (2)$$

For $\sigma \ll \delta z = (z_2 - z_1)$, one obtains the number density in each bin. Partitioning atom contributions by volume thus acts as a smearing factor. An equivalent analysis is obtained by convoluting the atom position distribution, $f(z)$, with the function $g(u)$ for spheres:

$$f(z) = \sum_{i=1}^{n} \delta(z - z_i) \tag{3}$$

$$g(u) = \begin{cases} 0 & -\infty < u < -\dfrac{\sigma}{2} \\ \pi\left(\dfrac{\sigma^2}{4} - u^2\right) & -\dfrac{\sigma}{2} < u < \dfrac{\sigma}{2} \\ 0 & \dfrac{\sigma}{2} < u < \infty \end{cases} \tag{4}$$

The resulting convolution is

$$\rho(z) = \pi \int_{-\sigma/2}^{\sigma/2} \sum_{i=1}^{n} \delta(z - z_i - u)\left(\frac{\sigma^2}{4} - u^2\right) \mathrm{d}u \tag{5}$$

which is readily evaluated using Simpson's formula. Figure 4 illustrates $\rho(z)/\rho_0$ using $\sigma \ll \delta z$, i.e., number density rather than partitioning by volume; the result is very similar to the "fine-grained" density profiles reported by Huitema et al.[32] for the interface between crystal and melt in simulations of Lennard-Jones fluids. In this work, we choose to report results assuming a van der Waals volume for each site typical of the CH_2 group ($\sigma = 3.94$ Å).

Orientational order is characterized by the bond orientation parameter, defined as

$$S(z) = (3 \cos^2 \phi(z) - 1)/2 \tag{6}$$

$\phi(z)$ is the angle measured by a bond chord (the segment joining the midpoints of two consecutive bonds) centered at z, with respect to the z-axis. For example, for an all-trans crystal stem parallel to the z-axis, as in the {001} interphase, $\phi(z) = 0$ and $S(z) = 1$. In the amorphous region, $S(z) = 0$. The order parameter profile is obtained by convolution with $g(u)$ of the function $S(z)$, summed over all chords and configurations, analogous to density.

Lateral structure in the interphase is characterized using the 2D pair distribution function, $g_{2D}(r)$. For a particular bin of thickness δz located a distance z from the crystal lamella, $g_{2D}(r)$ is given by

$$g(r,z,\delta z) = \frac{A}{2\pi r \delta r} \frac{\langle n_r(r,z,\delta z)\rangle}{\langle n(z,\delta z)\rangle^2} \tag{7}$$

A is the area of the bin, $2\pi r\delta r$ is the incremental cylindrical area, $n_r(r,z,\delta z)$ is the number of atom pairs in the bin separated by a distance between r and $r + \delta r$, and $n(z,\delta z)$ is the total number of atoms in the bin.

To determine the interfacial energy, we first computed the "bin energy", resulting from the interaction of all the atoms in a bin with the rest of the interphase. As with the total energy calculation, a tail correction was applied for interactions beyond the cutoff radius.[29,33] We then constructed a cumulative energy plot, starting with the centerline bin and consecutively adding the energy of bins on both sides of it, until the crystal planes are reached. The resulting plot exhibits an initial linear region, whose slope corresponds to the energy per atom in the amorphous region, followed by a transition to a second linear region whose slope corresponds to the energy per atom in the crystal region. We computed the slope of this curve from each pair of points, divided by area to obtain an interfacial energy per atom, and plotted it versus the cumulative number of atoms. To obtain the total potential energy of the interface, we integrated the area under the curve in the region lying between the amorphous and crystal regions. Because of some uncertainty in defining the precise bounds of the interfacial zone, computed interfacial energies are estimated to be accurate to ±10%.

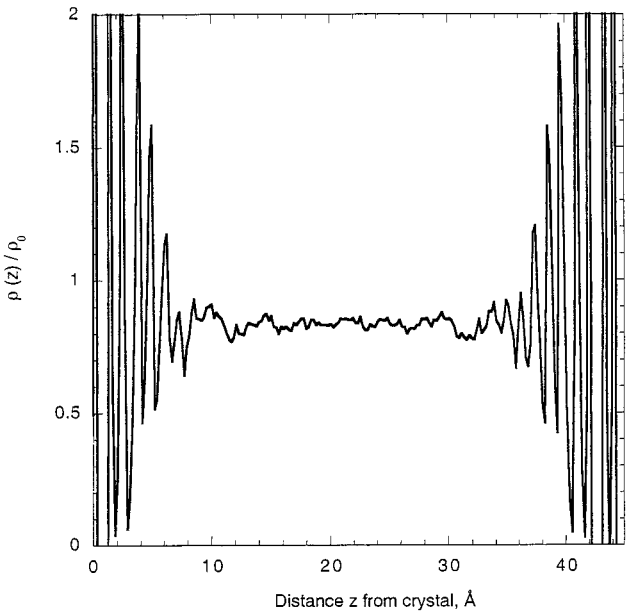

Figure 4. Normalized density distribution as a function of the distance from crystal, for $\sigma = 0.05$ Å and $\delta z = 0.13$ Å. The entire interphase is shown without symmetrization about the centerline; both crystal boundaries are evident, near 0 and 45 Å.

To characterize interfacial entropy, we analyzed the length distribution of chain populations in the interphase. The changes in connectivity brought about by the Monte Carlo moves result in an equilibrium distribution of chain lengths, subject to excluded volume and crystal order at the lamellar surfaces. We have previously reported a Gaussian model for chain length distributions between two smooth plates, without excluded volume interactions.[34] The partition function for such a system of noninteracting chains can be written down as the product of the partition functions of individual populations:

$$Y = \sum_{m=1}^{n} (N - N_T)! N_T! \prod_{K=\{L,B,T\}} \prod_{k=1}^{m} \frac{Z_K(D,k)^{K_k} \exp(\beta \mu_k{}^{*K})}{K_k!} \tag{8}$$

where the summation is over all possible distributions, consistent with the constraints of constant N (total number of chains), N_T (total number of tails), and n (total number of atoms) in the interphase. $Z_L(D,k)$, $Z_B(D,k)$, and $Z_T(D,k)$ are the configurational integrals of individual species (i.e., a chain of length k belonging to one of the three populations: tails T, loops L, or bridges B, subject to the constraints of separation distance D between the crystals). K_k is the number of chains of length k in population K. Setting $\mu_k^* = 0$ and assuming a Gaussian chain model for species allows one to obtain the following equations for $Z_K(D,k)$:

$$Z_L(D,k) = \sum_m \exp\left(-\frac{6m^2D^2}{kC_k{b_0}^2}\right)\left[1 - \frac{12m^2D^2}{kC_k{b_0}^2}\right]$$

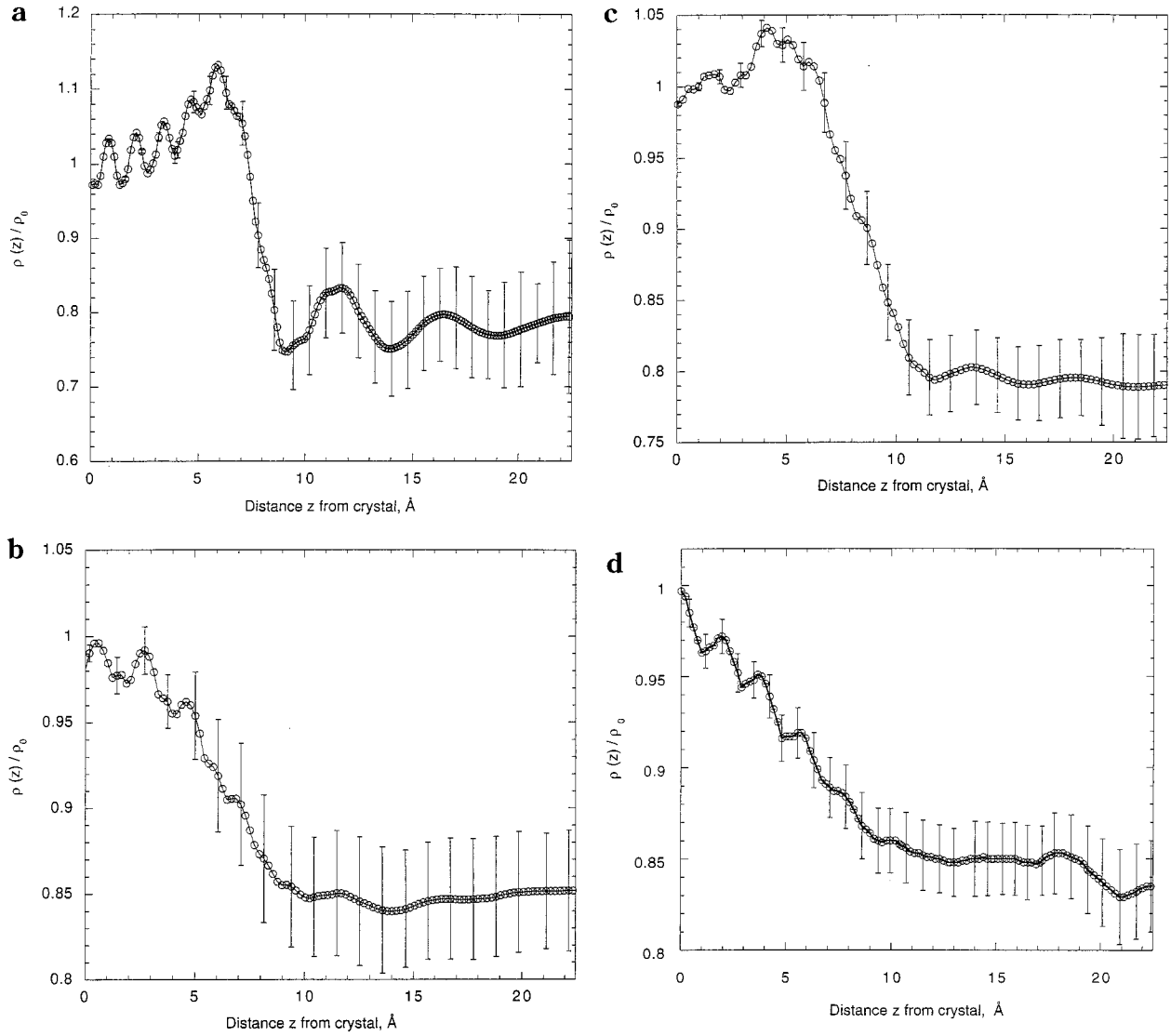

Figure 5. Normalized density distribution of interphases. ρ_0 is the density of the crystal region. Simulation data for each bin is shown as circles, while the solid lines serve as guides to the eye. Error bars indicating one standard deviation are shown at intervals of five bins. For the calculations, $\sigma = 3.94$ Å and $\delta z = 0.13$ Å. The curves are symmetrized about the centerline of the simulation. (a) {001}; (b) {101}; (c) {201}; (d) {502}.

$$Z_B(D,k) = \sum_m \exp\left(-\frac{3D^2(1-2m)^2}{2kC_k{b_0}^2}\right)\left[\frac{3D^2(1-2m)^2}{kC_k{b_0}^2} - 1\right]$$

$$Z_T(D,k) = \sum_m \exp\left(-\frac{6m^2D^2}{2kC_k{b_0}^2}\right) - \exp\left(-\frac{3D^2(1-2m)^2}{2kC_k{b_0}^2}\right) \quad (9)$$

b_0 is the bond length, and C_k is the stiffness constant for a chain of length k. These equations illustrate the exponential nature of the ideal Gaussian chain length distributions.

4. Results and Discussion

Results of the simulations reveal the thermodynamic properties for a metastable interphase subject to different degrees of chain tilt. The effect of chain tilt on the structure of the interphase is also reported. The characterization of the interface through density, orientational order, transverse structure, and dihedral angle distribution is reported first, followed by results on the potential energy and entropy. For the sake of brevity, we focus on results for the {201} interphase whenever possible. In most cases, the behaviors of {101} and {502} interphases are qualitatively similar and may be deduced therefrom.

4.1. Characterization of the Interface. *Density.* The density profiles along the *z*-direction for the {101}, {201}, and {502} interphases are shown in Figure 5, along with that of the {001} interphase from ref 2, for comparison. The mild oscillations near the crystal boundaries are remnants of the regularly arranged atoms in the crystal layers in the presence of convolution with bead volume. Near the centerline of the simulation in each case, the density is relatively constant at the amorphous value, within the statistical uncertainty of the simulations. In between these two regions is the interfacial region, where the density decrease signals the transition from crystal to amorphous structure. For all the interphases studied, this region is found to be approximately 10−12 Å thick. In the {001} interphase, there is a sharp peak in the density profile about 6 Å from the crystal surface, where the normalized density

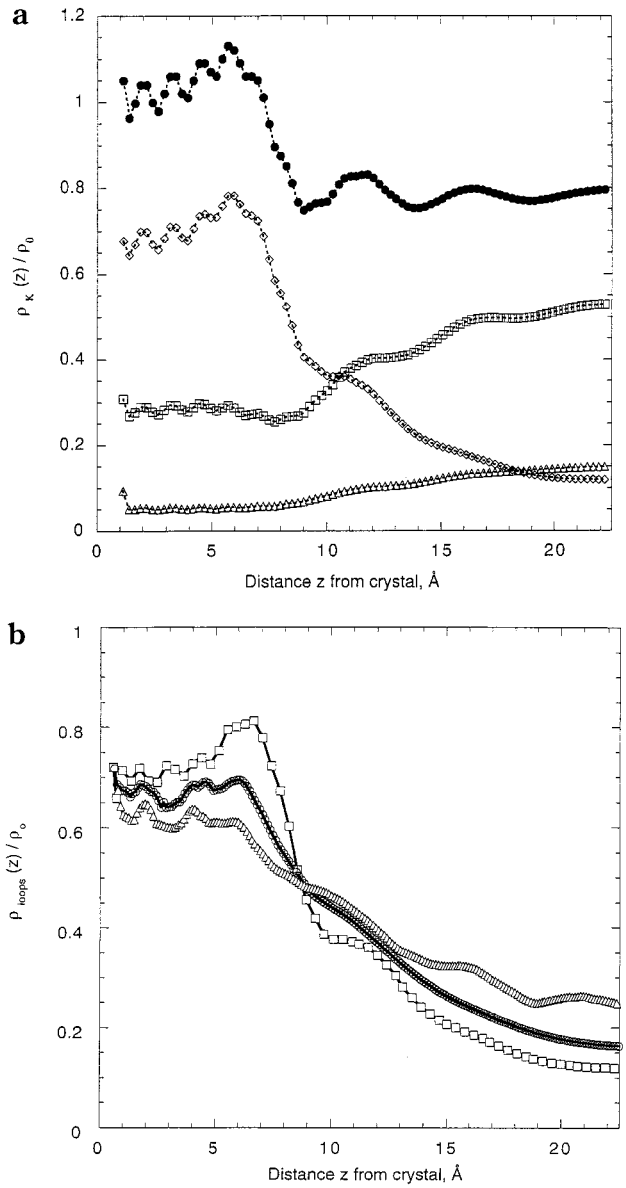

Figure 6. Contributions of chain populations to interphase density. (a) Different populations in the {201} interphase: K = loops (diamonds), bridges (triangles), tails (squares), total (filled circles). (b) Loop populations for different interphases: {001} (squares), {201} (circles), {502} (triangles}. $\sigma = 3.94$ Å and $\delta z = 0.13$ Å.

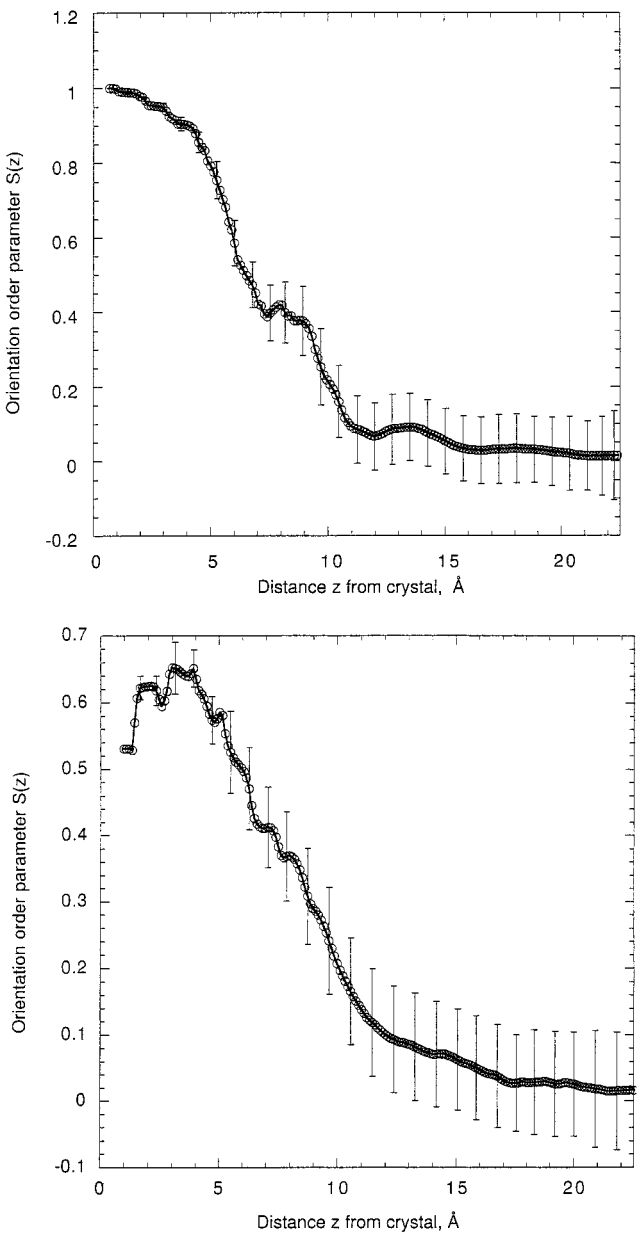

Figure 7. Bond orientation order parameter $S(z)$ for different interphases. Data points are shown as circles for each bin. Solid lines serve as guides to the eye. Error bars indicating one standard deviation, are shown at intervals of five bins. (a) {001}; (b) {201}.

increases to about 1.1. This peak is associated with an increase in the number density of atoms in that plane. The intensity of this peak is weaker in the {101} interphase and disappears altogether in the {201} and {502} interphases. Figure 6a shows the individual contributions to density from loops, bridges, and tails in the {201} interphase. The highest contribution in the interface region, particularly near 6 Å, is from loops, while tails and bridges contribute more to the amorphous region. Figure 6b shows a comparison of the contribution to density from the loop populations for each of the {001}, {201}, and {502} interphases. This demonstrates that the density peak observed in the {001} interphase is attributable to loops.

Bond Orientation Parameter. Density is only one measure of the change in structure across the interface. For orientational order, the bond orientation parameter for {001} and {201} interphases is shown in Figure 7. For the {001} interphase, the order parameter starts at unity and then decays smoothly to zero, interrupted only by a characteristic drop near 6 Å, due to the presence of a plane where most of the bond chords are oriented parallel to the crystal surface. For the {201} interphase, the bond order parameter starts at a value of 0.52, characteristic of the chain tilt in the crystal. Initially, it increases slightly as the chain direction turns, on average, toward the interface normal. The subsequent decay in the order parameter is then less severe than for the {001} case and is devoid of the drop observed in that case. The orientation parameter approaches zero in the middle of the simulation box consistently for all the interphases, signifying that the centerline is isotropic. The thickness of the interface as measured by the transition in orientational order is also about 12 Å for all the interphases studied, comparable to the thickness indicated by the density profiles in Figure 5.

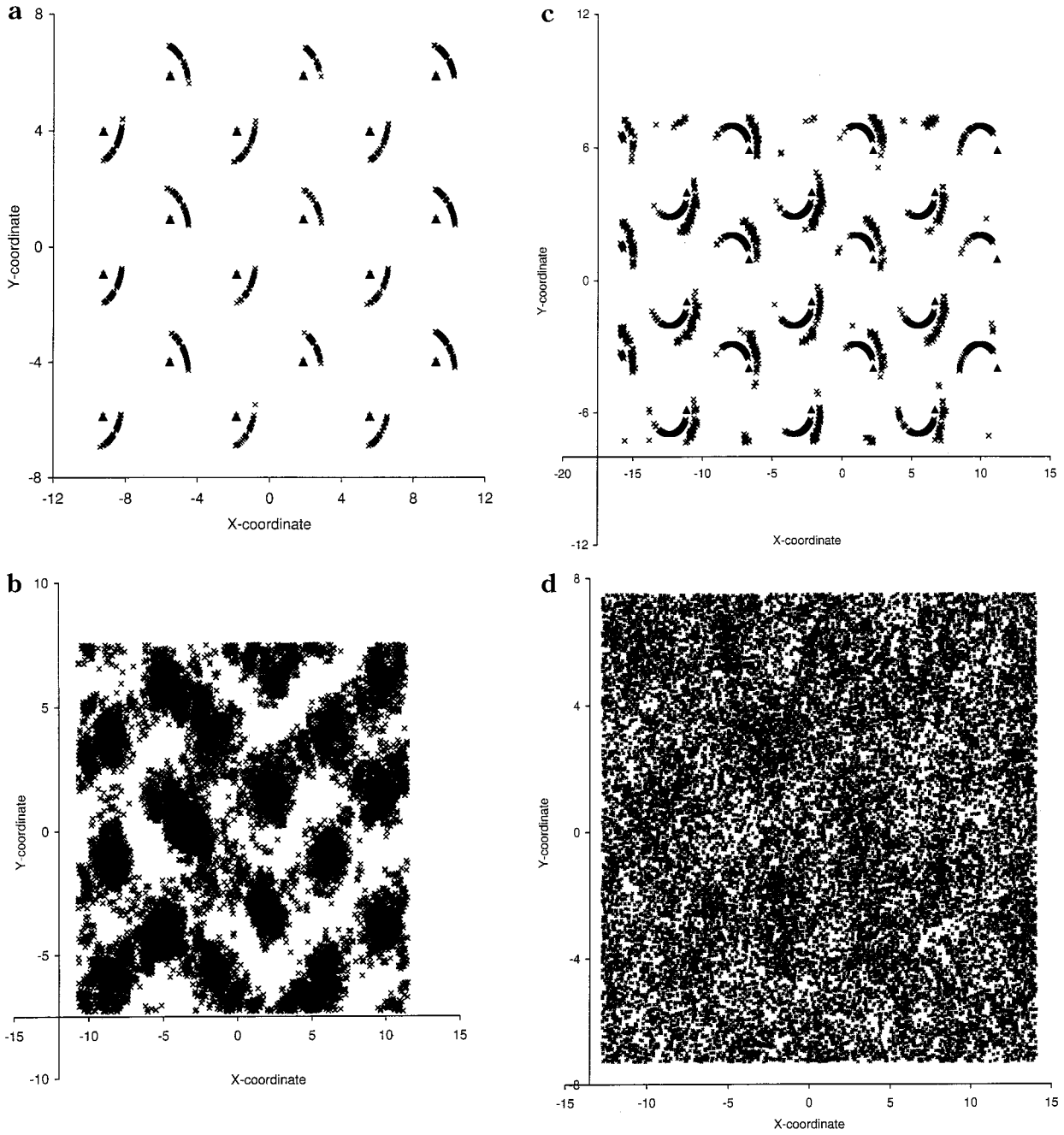

Figure 8. (a) Scatter plot of atoms positions for selected interphases and distances from crystal surface. Crosses indicate sampled atom positions; open triangles indicate axes of chains in crystal. (a) {001} interphase, $z = 2$ Å; (b) {001} interphase, $z = 6$ Å; (c) {201} interphase, $z = 6$ Å; (d) {201} interphase, $z = 15$ Å.

Transverse Structure. Transverse structure parallel to the crystal surface is examined in this section using scatter plots and pair distribution functions. Scatter plots show the positions sampled by the centers of atoms, throughout the entire simulation, at a particular distance from the crystal surface. Careful examination of the transverse structure reveals the manner in which disordering occurs in the interface. The scatter plot for the {001} interphase in a layer near the crystal boundary is shown in Figure 8a; in this figure, the atoms cluster in arcs around their mean positions, consistent with a rotational acoustic vibration mode characteristic of the crystal. The arcs are arranged in a manner consistent with little overlap of atoms. The scatter plot of the next layer, chosen near the plane at 6 Å, shows a high probability of atom centers located along the [110] direction (Figure 8b). As a representative for the tilted interfaces, Figure 8c shows the scatter plot taken at a distance of 6 Å from the crystal surface for the {201} interphase. The two sets of arcs observed in this case are due to rotational modes parallel to the chain axis which, due to chain tilt, result in contributions from two different atoms on each chain intersecting the plane. The structure suggested by Figure 8c is intermediate between that of Figures 8a and 8b; the arcs are less restricted than in Figure 8a but do not exhibit the kind of chain-to-chain crossover suggested by Figure 8b. Figure 8d shows a scatter plot from the {201} interphase located at a plane 15 Å from the crystal surface. It illustrates the fully amorphous structure characteristic at this z-distance of all the interphases studied.

The pair distribution functions at different bin locations are plotted in Figure 9a for the {201} interface. At 2 Å from the crystal surface, the pair distribution

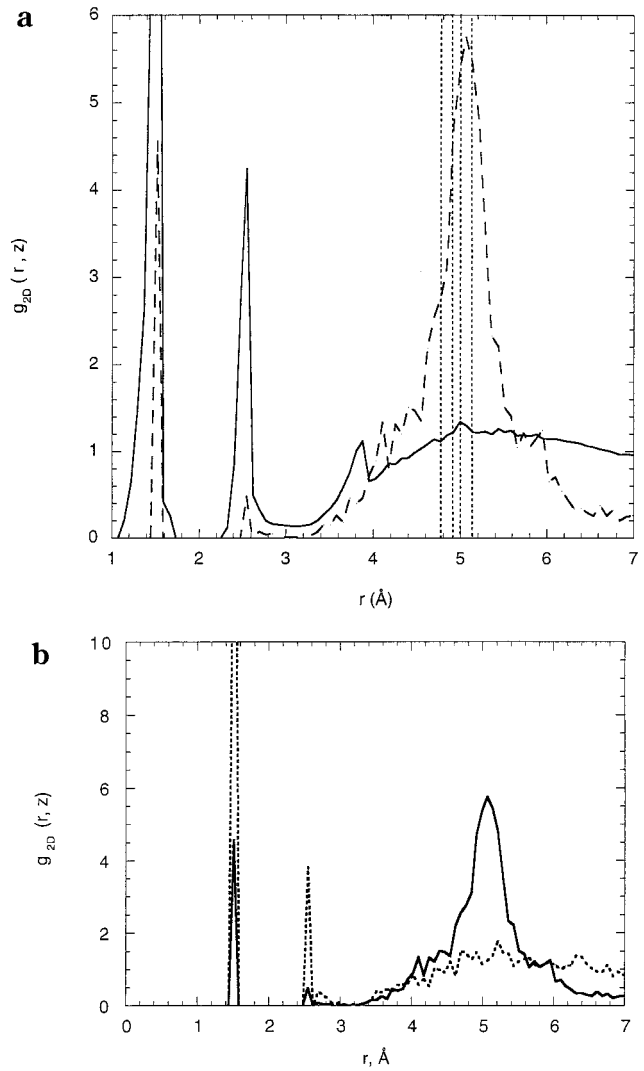

Figure 9. 2D pair distribution function for selected interphases and distances from crystal surface. (a) {201} interphase, $z = 2$ Å (dotted line), 6 Å (dashed line), and 15 Å (solid line); (b) $z = 6$ Å, comparison of the {001} interphase (dotted line) and the {201} interphase (solid line).

function shows two sharp peaks at 4.8 and 4.9 Å, characteristic of the intermolecular distances between carbon atoms in the orthorhombic crystal. At 6 Å from the crystal surface, two new peaks appear around 1.53 and 2.6 Å, corresponding to first- and second-neighbor intramolecular distances along a chain, indicative of chains running parallel to the crystal surface in this plane. At 15 Å, the 2D pair distribution function resembles that of an amorphous melt, with $g_{2D}(r)$ exhibiting intramolecular peaks at small r and approaching unity at large r. The pair distribution functions at 6 Å for the {001} and {201} interphases are compared in Figure 9b. These are consistent with the scatter plots; at this z-distance in the {001} interphase, numerous chains are oriented parallel to the crystal surface and join up neighboring chain positions, whereas in the {201} interphase disorder is introduced through less drastic excursions of chain direction from that in the preceding layer.

The results for density, orientational order, and transverse structure presented so far are all consistent with a change in interface structure and topology with increasing chain tilt. The {001} interface is characterized by a well-defined fold surface near $z = 6$ Å, at which

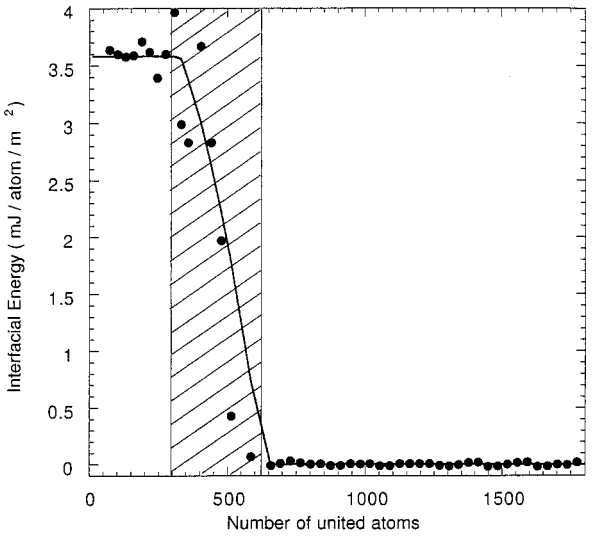

Figure 10. Interfacial energy per atom for the {201} interphase, plotted versus cumulative atom count from the centerline of the simulation. Solid circles represent simulation data. The fitted curve is obtained using five-point interpolation. Interfacial energy is computed from the area under the curve in the shaded region.

a large number of chains fold back into the crystal. The signature of this fold surface is seen in the peak in density, the drop in orientational order, and in the analysis of transverse structure, which indicates some fraction of chains running parallel to the crystal surface. The signatures are weaker for the {101} case and absent from the {201} and {502} results. Confronted by a large areal density (or flux) of chains exiting the crystal, the {001} and {101} interfaces generate a fold surface in order to reduce the flux to a level sufficient to accommodate disordering. With their lower areal density of chains, the {201} and {502} surfaces are able to accommodate disordering by more modest means, accumulating smaller deviations from the crystallographic chain direction and allowing loops to form throughout the entire interface.

4.2. Interfacial Energy. Figure 10 shows a plot of the interfacial energy per atom for the {201} interphase as a function of the cumulative number of atoms encountered from the simulation centerline, as described in section 3. The interfacial energy, relative to the crystal, is obtained from the area under the curve in the gray region. Values of 140, 100, 70, and 90 mJ/m^2 were computed for the {001}, {101}, {201}, and {502} interfaces, respectively. Even allowing for uncertainty in the determination of the interface boundaries, a pronounced minimum is observed around 35° tilt, corresponding to the {201} interphase. This optimum in energy is in excellent agreement with the experimental results of Basset et al.,[11] indicating crystal chains tilted predominantly around 35° from the lamellar normal, with smaller populations tilted around 15° and 45°, and still fewer showing 0° of tilt.

The significance of this optimum in interfacial energy is potentially profound. First, the good agreement between these simulations and experiments for polyethylene suggests that a model for the interlamellar phase based on a metastable equilibrium between crystal and melt may be at least qualitatively correct. Second, one consequence of the equilibrium nature of this model is that chain tilt in the real crystal, and the details of interfacial structure, topology, and energy,

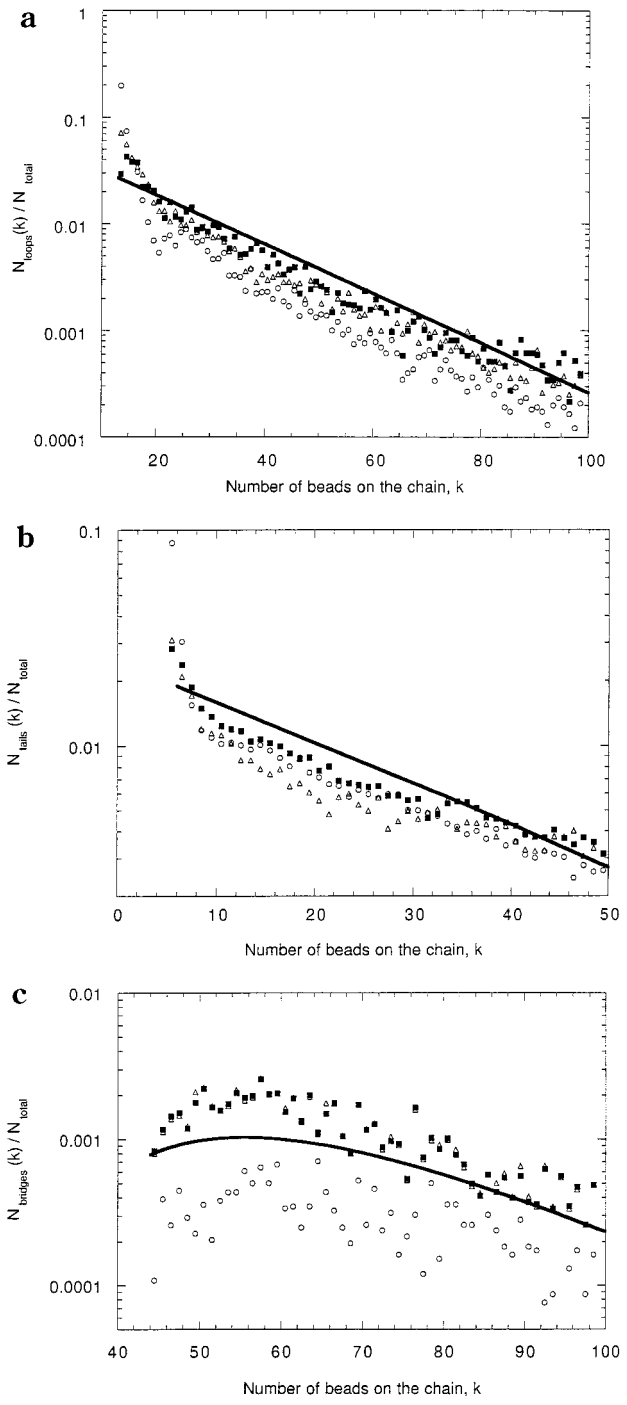

Figure 11. Semilog plots of the chain populations for the {001} (circles), {101} (triangles), and {201} (filled squares) interphases. Results for the Gaussian chain model is shown as solid line. (a) Loops; (b) tails; (c) bridges.

need not be a direct consequence of the mechanism of crystallization. Instead, they reflect the action of dynamic processes, ongoing both during crystallization and afterward, which permit local equilibration of the interlamellar phase, subject only to a relatively limited set of constraints imposed upon the morphology during crystallization.

Of course, the interfacial energy presented here is for freely rotating chains and does not include entropic effects explicitly. Qualitative arguments can be made that interfacial entropy also favors chain tilt and does not significantly alter the above conclusion; one such argument is offered below. Preliminary results for chains with realistic torsion potentials are qualitatively similar to these results for freely rotating chains and will be reported elsewhere.[29]

Table 1. Percentage of Chains in Loop, Bridge, and Tail Populations, for Interfaces Arising from Different Degrees of Chain Tilt; Also Indicated Is the Percentage of Loops That Appear as Tight Folds (with an End-to-End Distance ≤5 Å)

tilt angle (deg)	0	19	34.4	41
tails	43.5	43.5	43.5	43.5
bridges	2.2	4.0	6.1	7.1
loops	54.3	52.5	50.4	49.4
tight folds	83.6	77	47.3	24.4

4.3. Chain Length Distributions. The distribution of chain lengths within each population provides a partial indication of trends in interfacial entropy. For ideal chains with zero residual chemical potential and no excluded volume, the length distributions are exponential for both loops and tails and for bridges in the limit of long length; due to the fact that there is a minimum chain length that can form a bridge, the bridge population goes through a maximum before decaying exponentially. This is illustrated by the solid lines in Figure 11 for the Gaussian chain model. Constraints due to crystal structure, intramolecular conformation, and packing interactions can cause deviation from this exponential distribution. Parts a and b of Figure 11 show the length distributions for loops and tails, respectively, for the {001}, {101}, and {201} interphases. In each case, the effect of realistic constraints serves to increase the number of short loops and tails and to decrease the number of long loops and tails, relative to the ideal case. This deviation is particularly strong in the case of the {001} interphase; the number of short loops (i.e., "tight folds") is approximately 3 times that observed in the {201} interphases. This difference is attributed to the higher flux of chains from the crystal surface that must be dissipated at the {001} facet. The formation of numerous tight folds, or short loops, comes at the expense of loops of intermediate or long length. The result is a strong perturbation from the length distribution expected for an ideal amorphous melt of Gaussian chains. This perturbation comes at a cost in free energy (i.e., lower entropy), which is greater for larger perturbations from ideal.

Since the loop and bridge populations are in equilibrium with each other, one consequence of the shift to longer loops in the tilted-chain interphases is the concurrent decrease in the total number of loops (determined from the area under the curves) and an increase in the number of bridges. Figure 11c compares the bridge length distributions for {001}, {101}, and {201} interphases to the Gaussian model; from this, it is clear that the bridge population in {001} is suppressed for all chain lengths. The number fraction of chains in loop, bridge, and tail populations as well as the fraction appearing as tight folds are shown in Table 1 for each interphase studied.

Last, we look at the orientation of the end-to-end vector of the loops, to study the organization of loops at the crystal surface. A histogram of the angles formed by the end-to-end vector of each loop with respect to the {010} plane of the crystal is shown in Figure 12, for the {001} and {201} interphases. The nearest-neighbor reentry points for loops are in the [110] and [200] directions, approximately (35°, 145°) and 90°, respec-

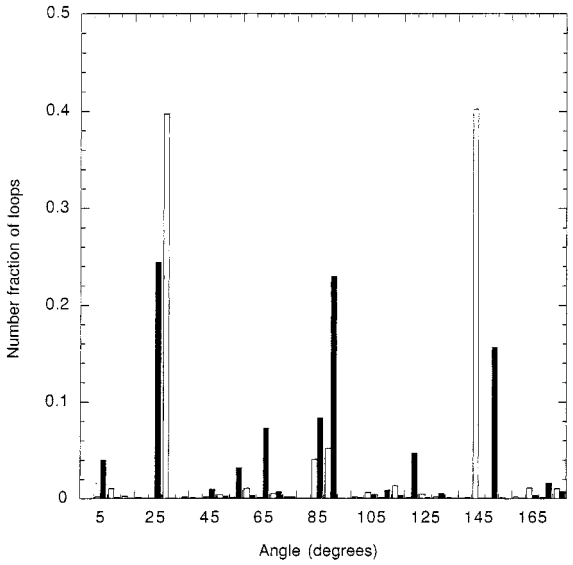

Figure 12. Loop reentry angle histogram: {001} interphase (open bars); {201} interphase (filled bars).

tively.[35] The next nearest reentry points are along the [010] and [310] directions, approximately 0° and (65°, 115°), respectively. For the {001} interphase, loops are observed to be mainly along the [110] direction, consistent with the formation of tight folds discussed earlier. As the tilt angle increases, the number of tight folds decreases, and the populations of [200] and [310] loops become prevalent.

5. Conclusions

The effect of chain tilt on the structure and interfacial energy of a semicrystalline polymer has been studied. All of our results for the {001} interphase point to the dissipation of chain flux through the development of short loops (folds), predominantly along the [110] direction. The resulting fold plane which arises at 6 Å is supported by a peak in density, a drop in bond orientational order, and the development of intramolecular contributions to the lateral structure in this layer of the interface. This tightly folded surface is disfavored both energetically, due to excluded volume overlap in the fold plane, and entropically, due to deviation from the ideal chain length distribution for loops. With increasing chain tilt, areal density per chain decreases, thereby lowering the tendency to form tight folds significantly. The total population of loops, including those that penetrate into the amorphous region, is reduced only slightly. Specifically, these results indicate that the role of chain tilt is to reduce excluded volume overlap and to permit dissipation of chain flux through a wider range of loop structures, including both longer loops and more varied topology. Significantly, this does not imply a thicker interface. Our simulations suggest that the total free energy is likely to be optimal for a chain tilt angle in the vicinity of 35°. To our knowledge, these simulations offer the first quantitative explanation for the predominance of lamellae with the {201} basal plane in the experimental studies of melt-crystallized polyethylene. Their success in this regard has important implications for our understanding of the structure of semicrystalline polymer solids and for the relevance of both thermodynamic and kinetic studies directed toward this goal.

Acknowledgment. This work was supported primarily by the MRSEC Program of the National Science Foundation under award number DMR 98-08941.

References and Notes

(1) Keller, A. *Philos. Mag.* **1957**, *2*, 1171.
(2) Balijepalli, S.; Rutledge, G. C. *J. Chem. Phys.* **1998**, *109*, 6523.
(3) Balijepalli, S.; Rutledge, G. C. *Macromol. Symp.* **1998**, *133*, 71.
(4) *Faraday Discuss. Chem. Soc.* **1979**, *68* and papers therein.
(5) Khoury, F. *Faraday Discuss. Chem. Soc.* **1979**, *68*, 404.
(6) Keith, H. D.; Padden, F. J., Jr. *Macromolecules* **1996**, *24*, 7776.
(7) Yoon, D. Y.; Flory, P. J. *Macromolecules* **1984**, *17*, 868.
(8) Mandelkern, L. *Acc. Chem. Res.* **1990**, *23*, 11, 380.
(9) Khoury, F.; Bolz, L. H. In *38th Annual Proceedings of the Electron Microscopy Society of America, San Francisco, CA*; Baily, G. W., Ed.; Claitors: Baton Rouge, LA, 1980; p 242.
(10) Bassett, D. C.; Hodge, A. M. *Proc. R. Soc. London* **1978**, *A359*, 121.
(11) Bassett, D. C.; Hodge, A. M. *Proc. R. Soc. London* **1981**, *A377*, 25.
(12) Bassett, D. C.; Hodge, A. M.; Holley, R. H. *Proc. R. Soc. London* **1981**, *A377*, 39.
(13) Bassett, D. C.; Hodge, A. M. *Proc. R. Soc. London* **1981**, *A377*, 61.
(14) Voigt-Martin, I. G. *J. Polym. Sci., Polym. Phys.* **1981**, *19*, 1769.
(15) Labaig, J. J. Ph.D. Thesis, University of Strasburg, 1978.
(16) Varnell, W. D.; Ryba, E.; Harrison, J. R. *J. Macromol. Sci., Phys. B* **1987**, *26*, 135.
(17) Keith, H. D.; Padden, F. J., Jr. *Polymer* **1983**, *25*, 28.
(18) Keith, H. D.; Padden, F. J., Jr.; Lotz, B.; Whittman, J. C. *Macromolecules* **1989**, *22*, 5.
(19) Lovinger, A. J.; Keith, H. D. *Macromolecules* **1996**, *29*, 8541.
(20) Dimarzio, E. A.; Guttman, C. M. *Polymer* **1980**, *13*, 733.
(21) Guttman, C. M.; Dimarzio, E. A. *Macromolecules* **1982**, *15*, 525.
(22) Flory, P. J.; Yoon, D. Y.; Dill, K. A. *Macromolecules* **1984**, *17*, 862.
(23) Kumar, S. K.; Yoon, D. Y. *Macromolecules* **1989**, *22*, 3458.
(24) Marqusee, J. A. *Macromolecules* **1989**, *22*, 472.
(25) Mansfield, M. L. *Macromolecules* **1982**, *15*, 525.
(26) Zuniga, I.; Rodrigues, K.; Mattice, W. L. *Macromolecules* **1990**, *23*, 4108.
(27) Frank, F. C. *Faraday Discuss. Chem. Soc.* **1979**, *68*, 7.
(28) Dodd, L. R.; Boone, T. D.; Theodorou, D. N. *Mol. Phys.* **1993**, *78*, 961.
(29) Balijepalli, S.; Rutledge, G. C. Manuscript in preparation.
(30) Kumar, S. K.; Szleifer, I.; Panagiotopoulos, A. Z. *Phys. Rev. Lett.* **1991**, *66*, 2935.
(31) Pant, P. V. K.; Theodorou, D. N. *Macromolecules* **1995**, *28*, 7224.
(32) Huitema, H. E. A.; Vlot, M. J.; van der Eerden, J. P. *J. Chem. Phys.* **1999**, *111*, 4714.
(33) Mansfield, K. S.; Theodorou, D. N. *Macromolecules* **1990**, *23*, 4430.
(34) Balijepalli, S.; Rutledge, G. C. *Comput. Theor. Polym. Sci.* **2000**, *10*, 103.
(35) Rigorously, the [110], [200], and [310] directions cited here apply only to projections on the {001} facet of the crystal; with tilting these indices change, e.g., to [102], [152], and [356] on the {201} facet, but this distinction is ignored in our discussion here, to avoid unnecessary complication.

MA0012503